Materials and Design 106 (2016) 60–68

Contents lists available at ScienceDirect

Materials and Design

journal homepage: www.elsevier.com/locate/matdes

Fabrication of Co–Cr–Mo endoprosthetic ankle devices by means of Selective Laser Melting (SLM)

E. Liverani [a], A. Fortunato [a,*], A. Leardini [b], C. Belvedere [b], S. Siegler [c], L. Ceschini [a], A. Ascari [a]

[a] Department of Industrial Engineering, Università di Bologna, Bologna, Italy
[b] Movement Analysis Laboratory and Functional–Clinical Evaluation of Prostheses, Istituto Ortopedico Rizzoli, Bologna, Italy
[c] Drexel University, Philadelphia, USA

ARTICLE INFO

Article history:
Received 22 March 2016
Received in revised form 19 May 2016
Accepted 20 May 2016
Available online 28 May 2016

Keywords:
SLM
Biomedical
Co–Cr–Mo powder

ABSTRACT

A study of Cobalt–Chromium–Molybdenum endoprosthetic ankle implant fabrication by means of SLM is presented, including process characterization and kinematic considerations. Process optimization is first performed on samples with simple geometry to maximize density and mechanical strength using Co–Cr–Mo powders. Parameters such as laser scanning velocity, laser power and scanning strategy are varied, amongst others. Mechanical tests and microstructural analyses are performed to define process parameter windows for fabrication of near full density prostheses with negligible microstructural defects. Prosthetic ankles, based on medical imaging and biomechanical modeling, are then manufactured and kinematically tested to confirm their functional integrity and performance.

1. Introduction

Traditional endoprostheses are used to replace articular surfaces in case of degenerative diseases in major human joints, particularly in locomotion apparatus such as the hip, knee or ankle. Although huge progress has been achieved in recent decades, failures and patient dissatisfaction continue to be reported for these replacements. Failures are mainly due to: 1) a mismatch with the original joint because prosthesis geometries are produced in a limited number of sizes and shapes; 2) non-physiological load transfer and adverse bone adaptation because of different mechanical properties of the bone and implant materials; and 3) implant mobilization due to unsatisfactory osteointegration or cementing. These issues are particularly critical for small joints like the ankle; in this case, since the incidence of arthritis is lower in comparison to other joints, a very limited number of prosthesis sizes are produced, leading to higher occurrence of adaptation problems. As a result of these considerations, personalization and biomechanically sound surfaces are active research fields in the design of prostheses, both for total and partial joint replacements, where the latter is necessary for focal osteocartilagineous defects. Nowadays, the design of customized prostheses is already possible by means of medical imaging, subject-specific joint models and computer-based surgical techniques. On the other hand, conventional manufacturing processes such as casting, cutting etc. still lead to unacceptable production costs. Manufacturing cost therefore represents the real barrier for wide diffusion of customized endoprostheses using traditional processes. In recent years, thanks to significant improvements in manufacturing technology and software, together with increasing availability of new powders, Selective Laser Melting (SLM) is gaining more consideration. With this technique, manufacturing costs are small and not heavily influenced by the number of components to be produced. By joining material in a layer-by-layer technique via fusion and re-solidification of fine metallic powders, SLM also allows for the manufacturing of complex and personalized prostheses with different and controlled porosity levels, also using innovative materials which facilitate osteointegration and bone adaptation [1] [2] [3]. Moreover, SLM offers a high level of control over the architecture of the manufactured component, ensuring reproducibility and enabling scaling-up and standardization [4].

For successful implementation of SLM in the fabrication of orthopaedic devices, however, several challenges must be overcome [5]. Prosthesis components manufactured by SLM are characterized by non-equilibrium physical, metallurgical and chemical properties. Careful control of process parameters is fundamental to ensure correct microstructure, dimensional accuracy, and mechanical properties [6] [7] [8] [9] [10] [11] [12].

The first part of the present paper is devoted to identifying the optimal process window for manufacturing of simplified SLM samples produced in Cobalt–Chromium–Molybdenum (CoCr). Density measurements, compression, hardness and tribological tests, as well as microstructural characterization, were performed on simplified samples to correlate process parameters to the resulting SLM component properties. SLM CoCr prototypes were then produced, exploiting the previously determined optimal process parameters. An original procedure was

* Corresponding author.
E-mail address: alessandro.fortunato@unibo.it (A. Fortunato).

http://dx.doi.org/10.1016/j.matdes.2016.05.083
0264-1275/

developed for the design of novel articular surfaces for the human ankle joint, based on morphological information taken from medical imaging and original biomechanical models. Finally, the SLM ankles were kinematically tested on the original cadaver specimens in order to assess the artificial joints' ability to replicate natural joint motion.

2. Simplified CoCr samples

2.1. Production of simplified SLM CoCr samples

The CoCr metallic powders used for the experimental campaign, whose chemical composition is reported in Table 1, were chosen according to ASTM F1537. They were spherical in shape with dimensions in the range 15–45 μm. All specimens were fabricated using a SISMA MYSINT100 system equipped with an Yb-Fiber laser with a maximum power of 150 W and a focused spot diameter of 50 μm. The samples were built in a chamber filled with nitrogen and a residual oxygen content of 0.2% in volume.

Table 1
Chemical composition [wt%] of the CoCr powders.

C	Cr	Co	Mn	Mo
≤0.04	27–30	Balance	≤1	5–7
Ni	Si	W	Al, Ti, O	Fe
≤0.5	≤1	≤0.2	≤0.10	0.75

Table 2
Experimental campaign for the production of SLM CoCr samples.

Parameter	Unit	Min/max value	
Power	W	90	126
Scan velocity	mm/s	700	1200
Hatch space	mm	0.05	0.07

The operating procedure for SLM fabrication began with a CAD drawing of the specimen saved in STL format. This file was then processed using a dedicated software package, MARCAM AutoFab, which subdivided the solid component in layers (Fig. 1). Process parameters and scanning strategy were then designed with the same software.

The scanning strategy was defined as a chessboard, in which each layer was divided into 3 mm × 3 mm square blocks. During fabrication, the laser melted powders in each block by scanning parallel lines, with the scanning direction perpendicular to that of adjacent blocks (Fig. 2a). With reference to Fig. 2b, the laser firstly melted the white then the black blocks, starting at the origin of the reference coordinate system. Each layer was rotated 45° with respect to the layers above and below. At the end of each melted layer the laser moved along the perimeter twice, with an offset equal to the hatch space.

The samples used for the compression tests were cylindrical in shape with a diameter of 12 mm and a height of 19.5 mm, in accordance with standards for compression tests. The experimental activities were designed as a three factor, two level and three repetition experiment, as summarized in Table 2, while the layer thickness was maintained constant as 0.02 mm.

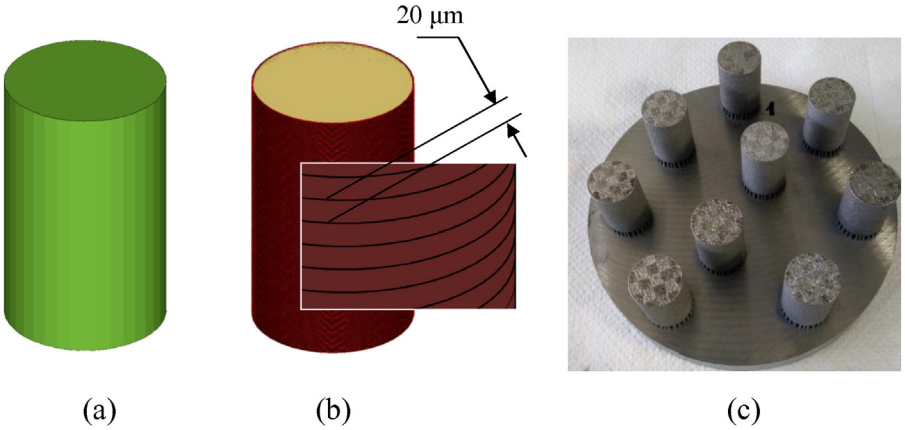

Fig. 1. Operation sequence for manufacturing of the compression specimens: STL file (a), division into layers (b) and final components (c).

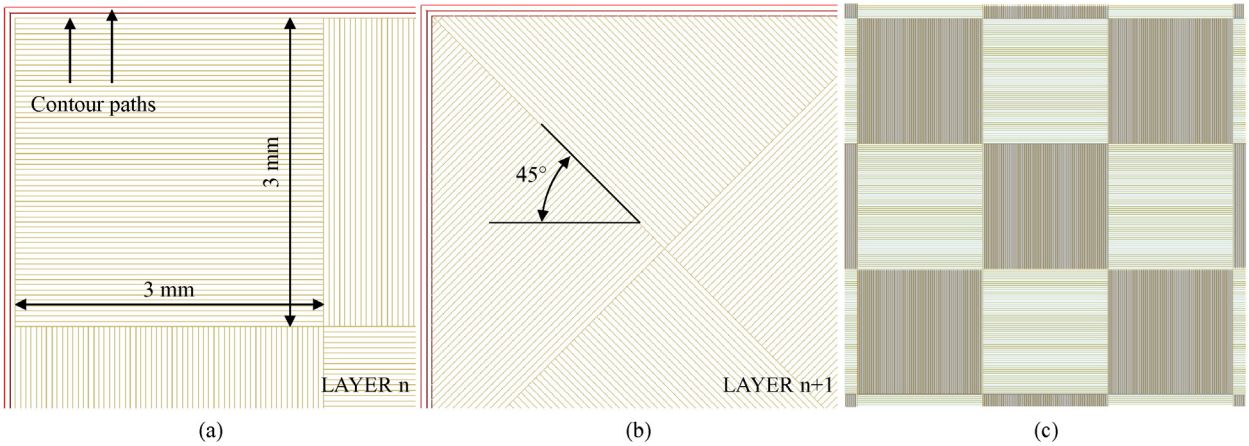

Fig. 2. (a) Chessboard laser scanning strategy and (b) block melting sequence.

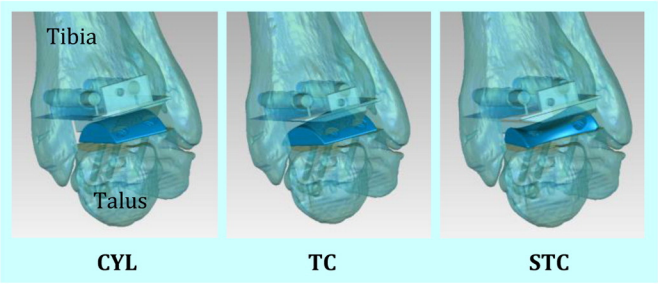

Fig. 3. 3D models of the replaced ankle with the three different designs, respectively CYL (left), TC (center) and STC (right). Each prosthesis comprises a tibial (above) and a talar (below) component.

Table 3
SLM parameters used for prosthesis manufacturing.

	Power [W]	Speed [mm/s]	Hatch space [mm]
Inner part	126	700	0.05
Outer part	90	1200	0.07

In order to verify the relationship between the process parameters and mechanical properties of the material, tensile specimens were also built with a 7 mm circular cross-section, 25 mm gauge length and a 5 mm transition radius between the gripped ends and the parallel length.

2.2. Experimental tests

All SLM samples were firstly subject to density tests performed by means of Archimedes' method in order to obtain an immediate comparison between the process parameters and the final density. Subsequently, the specimens were machined on a lathe to a final diameter of 11 mm for the compression specimens and 6 mm for the tensile specimens.

The compression samples were subjected to compression tests according to ASTM E9-09, by means of a hydraulic testing machine equipped with a 100 kN load cell. The strain rate was kept constant at $2.6 \cdot 10^{-4}\ s^{-1}$ throughout the tests, while the cross-head separation rate was 0.24 mm/min. The tensile samples were tested according to ISO 6892-1 by means of the same testing machine, using a cross-head separation rate of 1 mm/min. Strain was measured by a clip-on extensometer, with yield strength determined at a strain offset of 0.002. The extensometer gauge length was equal to 15.5 mm. Samples for metallographic analysis were mechanically ground with emery papers and polished with diamond suspension to 1 μm. To resolve the microstructural features, the SLM samples were electrolytically etched by applying a voltage of 4 V for 10 s in a solution containing 5 mL HCl and 10 g of ferric chloride diluted in 100 mL of distilled water. Microstructural characterization was carried out on selected samples with an optical microscope (OM) and a Scanning Electron Microscope (SEM) equipped with an Energy Dispersive Spectroscope (EDS). The tribological and hardness tests were carried out on some representative SLM samples, as reported in Section 4.1. Rockwell hardness tests were carried out using a diamond cone with a 150 kg load (HRC). Dry sliding wear tests were carried out on a flat-on-cylinder tribometer (block-on-ring contact geometry). Flat CoCr SLM specimens, $5 \times 5 \times 60\ mm^3$ in size, were used as stationary sliders, whilst the rotating cylinder, 40 mm in diameter, was SAE52100-EN100Cr6 steel, heat-treated to 63 HRC. Surface roughness of the mating materials was evaluated before the wear tests with a Hommelwerke T2000 stylus profilometer with a tip radius of 5 μm. Sliding tests were carried out at ambient temperature and humidity, under normal loads of 5, 10 and 30 N and at a sliding speed of 0.3 m/s over a sliding distance of 1000 m. During the tests, friction force and vertical displacement, which is related to total wear, were continuously measured by means of a load cell and a LVDT, respectively. The coefficient of friction (COF) and wear data were recorded as a function of the sliding distance. After the tests, the depth and width of slider scars were evaluated by stylus profilometry. Wear data were calculated according to ASTM G77-05. The morphology and composition of the wear scars on the sliders were analyzed by SEM to identify the dominant wear mechanisms.

3. Ankle prosthesis design and fabrication

3.1. Medical imaging and 3D prosthesis design

Among the major reasons for ankle endoprosthesis failure is non-anatomical geometry of the articulating surfaces, which is expected to result in unnatural motion and load-transfer at the replaced joint. Current designs have either cylindrical (CYL) or truncated cone (TC) articulating surfaces with a medial apex, the latter following an old biomechanical concept. A recent study by some of the present authors [13] using advanced medical image-based analyses and functional-based calculations, demonstrated that this concept is incorrect and that ankle articular surfaces can be better approximated by a saddle-shaped, skewed truncated cone (STC) with its apex originally directed laterally.

In order to test the effect of these novel articular surfaces on the resulting kinematics and load-transfer at the replaced ankle joint, a cadaver specimen was fully analyzed and corresponding prosthesis prototypes were produced with SLM. The specimen was first scanned by

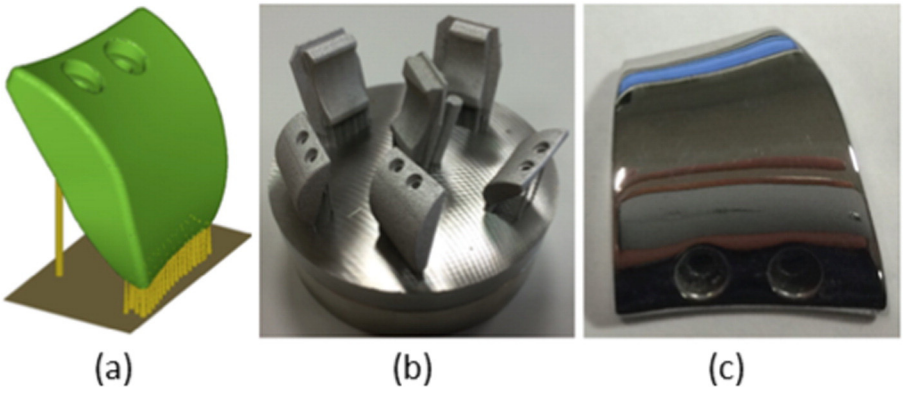

Fig. 4. a) Example of orientation in AutoFab of the talar component of the STC prosthesis; b) final arrangement of the STC, TC and CYL prosthesis components on the platform; c) example of the same talar component after the polishing.

Fig. 5. Cadaver specimen positioned in the testing rig during data acquisition; the ankle is replaced with one of the prototypes.

standard medical imaging instruments i.e. MRI and CT, and the image processing software Analyze DirectTM was used to obtain 3D models of bones and ligaments. From these models, the three custom-fit virtual articular surfaces were designed, i.e. CYL, TC and STC (Fig. 3).

3.2. Prosthesis fabrication

The 3D designs of the three custom-fit models obtained with Analyze DirectTM were tessellated as STL files and then imported into AutoFab post-processing software. Each prosthesis component was subdivided into two parts: a skin layer and a core volume. The inner part was manufactured using the optimum parameters from the results of density and mechanical tests (Section 4.1), whereas the process parameters for the outer skin were obtained using lower values of fluence to produce higher wear resistance (Section 4.1), see Table 3. The six prosthesis components were positioned by taking into account the gas flux and the motion of the coater, in order to limit oxide contamination and provide a homogeneous distribution of the powder for each layer. The skin layer was set to a thickness of 0.2 mm. Finally, each part of the components was manually polished before the kinematic tests in order to have a mirror finish, (Fig. 4).

3.3. Kinematical analysis

A thorough in-vitro experiment was conducted to test the ability of the prototype artificial surfaces to reproduce natural joint motion. Each of the three possible prosthesis designs was tested and compared with the natural anatomical articular surfaces.

The tibia was fixed to a special testing rig [14] and a stereophotogrammetric system (Stryker, Kalamazoo, MI-USA) tracked position and orientation of the tibia, talus and calcaneous via corresponding clusters of active markers and optoelectronic cameras, see Fig. 5. From these bone orientations, rotations were calculated for the ankle, i.e. tibio-talar, and subtalar, i.e. talo-calcaneal, joints. After motion measurements with the natural surfaces, each of the three prosthesis prototypes was implanted and tested separately by collecting five trials of full passive flexion–extension. Rotations about the three axes of motion, i.e. dorsi-/plantar-flexion(DP), inv-/ev-ersion (IE) and axial rotation (AR), were obtained throughout the flexion arc for both ankle and subtalar joints.

4. Results and discussion

4.1. Characterization of the simplified SLM CoCr samples

Figs 6–9 summarize the density and yield strength measurements performed on the cylindrical samples according to the experimental campaign reported in Table 2. Each value is the average of three

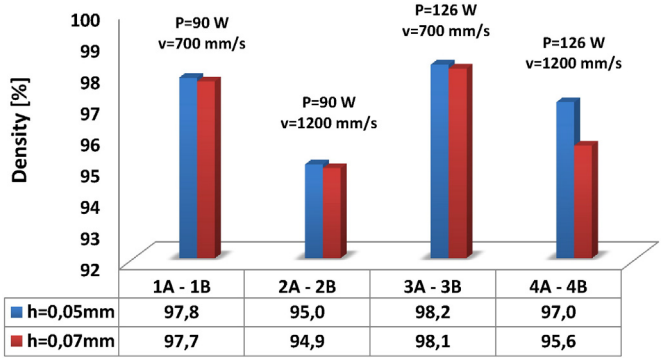

	1A - 1B	2A - 2B	3A - 3B	4A - 4B
h=0,05mm	97,8	95,0	98,2	97,0
h=0,07mm	97,7	94,9	98,1	95,6

Fig. 6. The influence of laser parameters and scanning strategy on sample density.

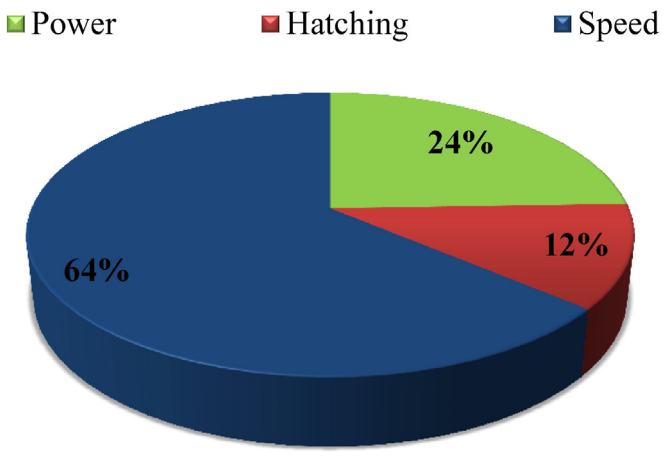

Fig. 7. Percentage influence of laser power, hatching and scanning speed on the final density of samples.

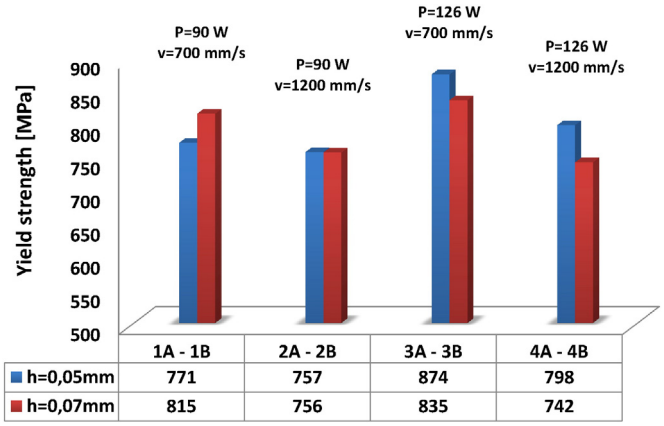

	1A - 1B	2A - 2B	3A - 3B	4A - 4B
h=0,05mm	771	757	874	798
h=0,07mm	815	756	835	742

Fig. 8. Influence of laser power, scanning speed and hatch space on compression yield strength of SLM samples.

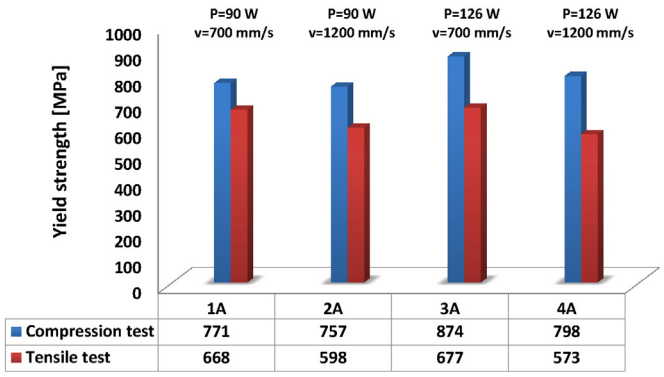

	1A	2A	3A	4A
Compression test	771	757	874	798
Tensile test	668	598	677	573

Fig. 9. Comparison between the yield strength of SLM samples obtained with compression and tensile tests.

repetitions. The sample density is defined as a percentage with respect to a reference value of 8.3 g/cm^3 for full density CoCr [15]. It is evident that defining the fluence [J/mm^3] as the ratio P/(v·h·t), P being the laser power, v the scanning speed, h the hatch space and t the layer thickness, the highest densities are obtained with maximum fluence (test condition 3) while the minimum density is obtained in test condition 2, where the lowest fluence was utilized. In test 4, the samples with h = 0.05 mm show high density, comparable with test 1, whereas with h = 0.07 mm a significant density reduction is evident due to an insufficient fluence.

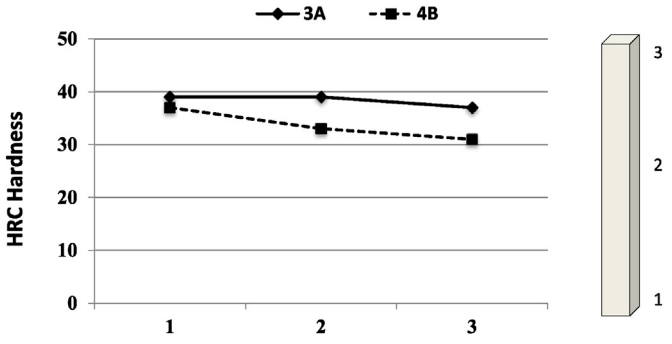

Fig. 11. Comparison between the hardness of SLM samples.

At fixed laser power, lower scanning speed leads to higher density. The influence of laser power seems lower at lower scanning speed. Hatch spacing has a significant effect on density only at the highest laser power and scanning speed. The influence of each parameter was evaluated individually; the resulting percentage is reported in Fig. 7. Laser scanning speed is the most significant cause of density variation, followed by the laser power. The hatch space, in the range of tested values, has the least influence.

Compression test results, reported in Fig. 8 confirm the same trend as those in Fig. 6; that is, test condition 3 with 0.05 mm hatch spacing represents the most suitable parameter range, leading to an average yield strength of 874 MPa. In general, test condition 4 gives more variable results, suggesting a minimum permissible fluence level of approximately 105 [J/mm^3], under which the process deteriorates. Test condition 2, below this minimum fluence, leads to low density and yield strength, while test conditions 1, 3 and 4 with h = 0.05 mm, above this value, give high density and yield strength.

Tensile tests results show lower values of the yield strength compared to compression tests but they evidence similar mechanical behavior (Fig. 9). The latter also confirmed that higher mechanical strength is obtained with test condition 3.

Representative optical micrographs of samples 3A and 4B are reported in Fig. 10 (a and b), respectively, showing the typical microstructural features of metallic materials produced by SLM, characterized by melt pools and solidification defects similar to those of laser welding [16].

These samples represent the best and worst obtained results, respectively. It is worth noting the presence of many solidification defects in sample 4B (Fig. 10b) resulting in low density and hardness. In fact, the hardness was equal to 38 ± 1.2 HRC for sample 3A and 36 ± 1.5 HRC for sample 4B. The hardness measurements in 3 different points of samples 3A and 4B are reported in Fig. 11, being point 1 the closest to the

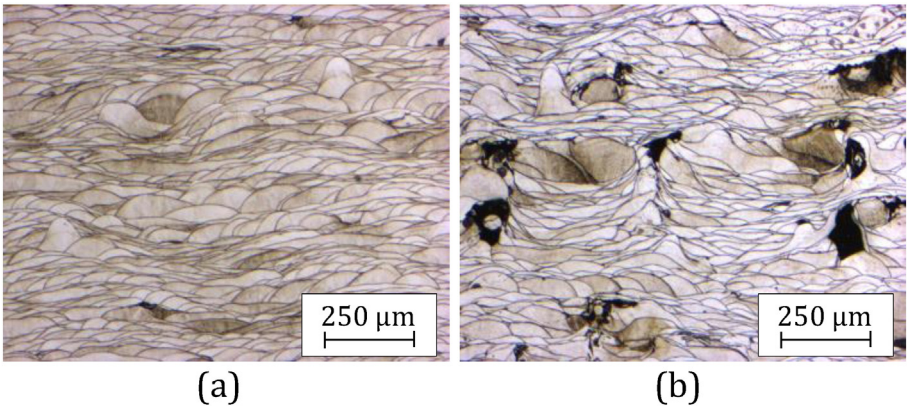

Fig. 10. Optical micrographs of sample 3A (P = 126 W, v = 700 mm/s, h = 0.05 mm) (a) and sample 4B (P = 126 W, v = 1200 mm/s, h = 0.07 mm) (b).

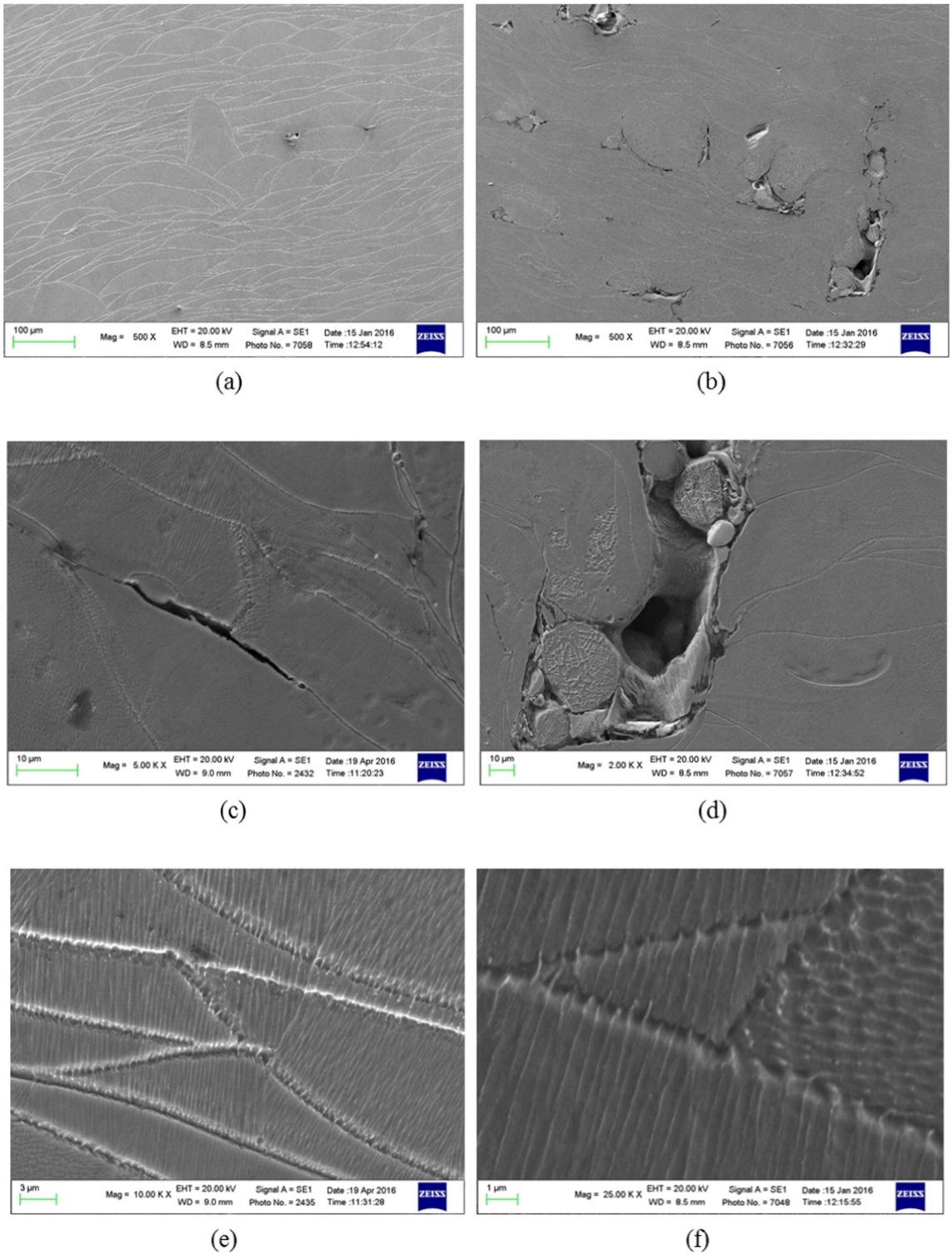

Fig. 12. SEM micrograph of sample 3A (P = 126 W, v = 700 mm/s, h = 0.05 mm) (a) and sample 4B (P = 126 W, v = 1200 mm/s, h = 0.07 mm) (b–f).

platform. In Section 4.2 the hardness measurements performed on the final prostheses are presented, confirming the values of sample 3A.

SEM images at higher magnification are reported in Fig. 12, confirming the presence of large pores, cracks and oxides in sample 4B. Typical causes of porosity in SLM processed parts are insufficient/incomplete melting (lack of fusion), entrapment of gas by surface turbulence, and shrinkage. Due to the irregular and elongated shape, the large pore in Fig. 11 (b,d) is most likely due to lack of fusion porosity. This type of defect is strongly dependent on processing parameters, such as laser power, layer thickness, scanning speed, scan spacing and fluence. The large porosity observed in sample 4B with respect to sample 3A can be related to the different fluence values utilized (75 J/mm^3 vs. 180 J/mm^3). Cracks, mainly dependent on energy density and consequent residual stresses [16], can also be observed.

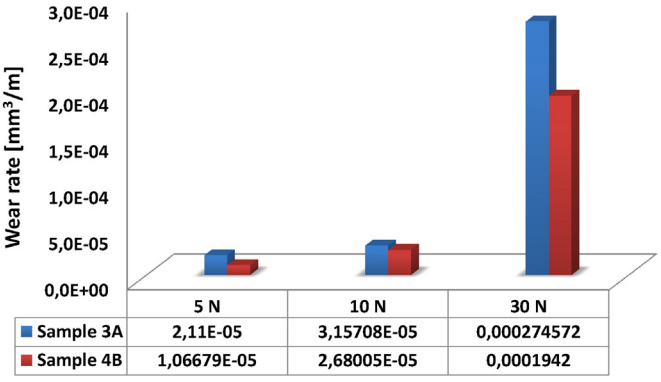

Fig. 13. Wear rate as a function of normal load for samples 3A and 4B at fixed sliding speed (0.3 m/s) and sliding distance (1000 m).

The typical cellular network microstructure formed by the high solidification rate and high level of non-equilibrium conditions achieved in the SLM process is shown in the SEM images, at higher magnification, in Fig. 12 e–f. The shape of the cellular structure is equiaxed or elongated (Fig. 12-f), depending on the relative orientation between the growth direction and section plane. It should be noted that the observed cell size ranges between 0.5 and 1 μm, typical of SLM metallic parts.

The results of dry sliding wear tests are shown in Fig. 13, where the wear rate (wear volume/sliding distance) at the different normal loads is shown. Wear rate increases with increasing normal load, as expected by Archard's law for sliding wear. Low wear rate values, typical of a mild oxidative wear regime, were displayed by both samples 3A and 4B.

The slightly higher wear rate of sample 3A at 30 N is probably due to an increase in the abrasive component due to its higher hardness. The occurrence of a mild triboxidative wear regime, in the tested range of normal loads, was confirmed by SEM/EDS analyses of the worn surfaces, showing a wear track fully covered by a compact oxide transfer layer at both low (Fig. 14a, 5 N) and high (Figure 14b, 30 N) load.

4.2. Kinematic and mechanical test results

In the in vitro tests, a repeatable intra-specimen path of motion was observed in the natural ankle and also after joint replacement, both at the ankle and subtalar joints, with the mean standard deviation over the five repetitions being smaller than 1° for all three anatomical axis rotations.

The observed mean ranges of motion before and after implantation of the 3D printed metal prototypes for the two joints and the three rotations (Table 4 and Fig. 15) were consistent with the literature [6].

Table 4
Experimental range of motion at the natural joints and after implantation of the CYL, TC and STC prostheses; mean ± standard deviation over the five repetitions.

Joint	Status		DP [°]	IE [°C]	AR [°C]
Ankle	Natural		32.9 ± 0.8	2.9 ± 0.3	3.8 ± 0.1
	Implant	CYL	33.6 ± 0.5	2.4 ± 0.1	3.2 ± 0.2
		TC	34.7 ± 0.8	2.6 ± 0.3	4.3 ± 0.2
		STC	33.0 ± 1.0	2.7 ± 0.3	2.7 ± 0.2
Subtalar	Natural		0.8 ± 0.0	4.3 ± 0.2	2.4 ± 0.2
	Implant	CYL	1.0 ± 0.1	3.7 ± 0.3	2.5 ± 0.2
		TC	0.8 ± 0.1	2.5 ± 0.2	2.2 ± 0.6
		STC	0.8 ± 0.0	2.9 ± 0.4	1.8 ± 0.1

Good restoration of natural motion was detected by looking at the ankle joint patterns (Fig. 15). This applied particularly for DP; in the other two rotations slight differences were observed as associated with the different prosthesis designs.

Finally, Fig. 16 shows the microhardness of the TC and the STC prostheses. The reported values refer to the longitudinal measurements performed 500 μm below the surface at intervals of 1mm along the length. The hardness values measured in the vertical direction, determined at the center of each prosthesis, exhibit the same values. These results confirm homogeneity in the heating cycle and the microstructure in whole the prostheses.

5. Conclusions

The present paper reports results obtained following the fabrication of three Cobalt–Chromium–Molybdenum endoprosthetic ankles by means of Selective Laser Melting. The fabrication of simplified samples was first carried out so as to define the optimal process parameters able to produce prosthesis components with proper microstructure, high density, good mechanical strength and wear resistance. A minimum laser fluence was defined, below which material density and yield strength were found to deteriorate significantly. Best results were obtained for treatment of CoCr with a laser power of 126 W, laser scanning speed of 700 mm/s and hatch spacing of 0.05 mm, corresponding to a fluence of 180 J/mm^3, for the inner part and 90 W, 1200 mm/s and 0.07 mm, corresponding to a fluence of 75 J/mm^3, for outer surface. These process parameters were then used to reproduce three possible ankle prosthesis designs having cylindrical, truncated cone surfaces with a medial apex and a saddle-shaped skewed truncated cone with lateral apex, currently fabricated with traditional microcasting. The subsequent kinematic tests, carried out on a cadaver leg revealed that the custom-fit articular surfaces reproduced natural joint motion well, further supporting the necessity of SLM for patient personalization in total ankle replacement.

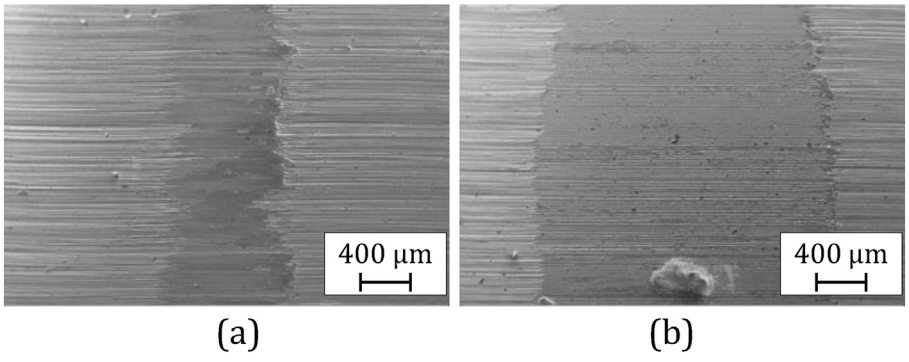

Fig. 14. SEM micrographs of the worn surfaces on sample 3A, tested at 5 N (a) and 30 N (b).

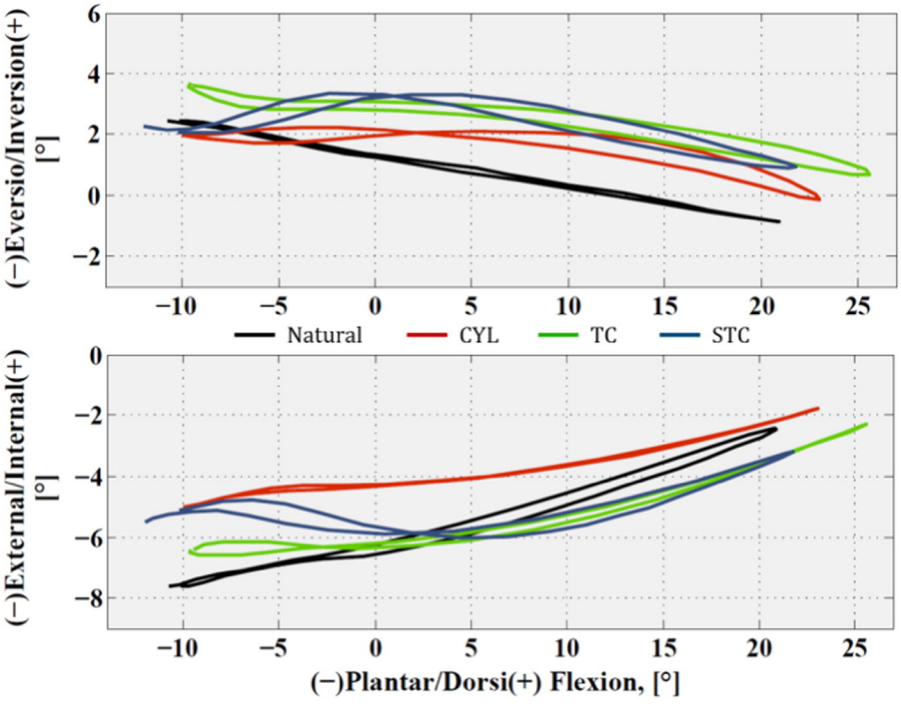

Fig. 15. Ankle rotation patterns (IE and AR versus DP)

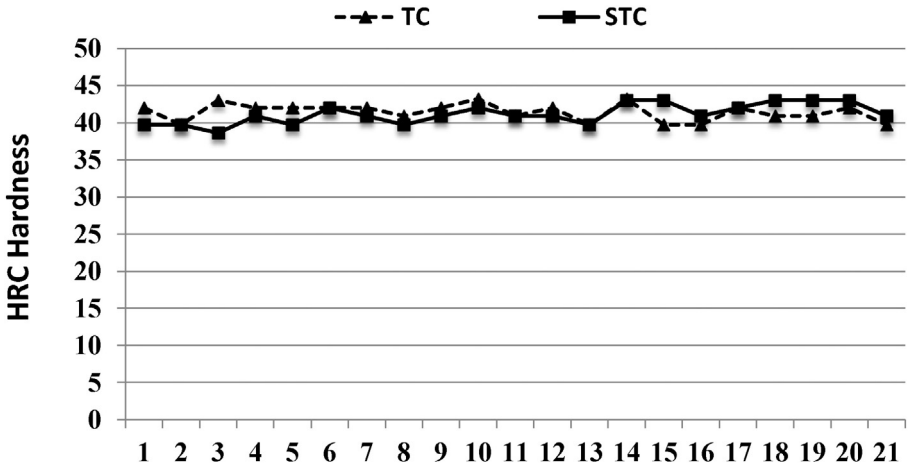

Fig. 16. Hardness measured on TC and STC prosthesis in longitudinal direction 500 μm below the surface.

References

[1] P. Bartolo, J.F. Kruth, J. Silva, G. Levy, A. Malshe, K. Rajukar, M. Mitsuishi, J. Ciurana, L. Ming, Biomedical production of implants by additive electro-chemical and physical processes, CIRP Ann. Manuf. Technol. 61 (2) (2012) 635–655.

[2] S.Y. Sing, W.Y. Yeong, F.E. Wiria, Selective laser melting of titanium alloy with 50 wt% tantalum: microstructure and mechanical properties, J. Alloys Compd. 660 (2015) 461–470.

[3] L. Zeng, N. Xiang, B. Wei, A comparison of corrosion resistance of cobalt–chromium–molybdenum metal ceramic alloy fabricated with selective laser melting and traditional processing, J. Prosthet. Dent. 112 (2014) 1217–1224.

[4] D.D. Gu, W. Meiners, K. Wissenbach, R. Popeawe, Laser additive manufacturing of metallic components: materials, processes and mechanisms, Int. Mater. Rev. 57 (3) (2012) 133–164.

[5] A.M. Khorasani, I. Gibson, M. Goldberg, G. Littlefair, A survey on mechanisms and critical parameters on solidification of selective laser melting during fabrication of Ti–6Al–4V prosthetic acetabular cup, Mater. Des. 103 (2016) 348–355.

[6] R. Wauthle, J. van der Stok, S.A. Yavari, J. Van Humbeeck, J.F. Kruth, A.A. Zadpoor, H. Weinans, M. Mulier, J. Schrooten, Additively manufactured porous tantalum implants, Acta Biomater. 14 (2015) 217–225.

[7] A. Takaichi, N.T. Suyalatu, J. Natsuka, N. Naoyuky, T. Yusuke, M. Satoshi, H. Doi, S. Kurosu, A. Chiba, N. Wakabayashi, I. Yoshimasa, T. Hanawa, Microstructures and mechanical properties of Co–29Cr–6Mo alloy fabricated by selective laser melting for dental application, J. Mech. Behav. Biomed. Mater. 21 (2013) 67–76.

[8] J.P. Kruth, G. Levy, F. Klocke, T.H.C. Childs, Consolidation phenomena in laser and powder-bed based layered manufacturing, CIRP Annal. Manuf. Technol. 56 (2) (2007) 730–759.

[9] A. Yadollahi, N. Shamsaei, S.M. Thompson, D.W. Seely, Effects of process time interval and heat treatment on the mechanical and microstructural properties of direct laser deposited 316L stainless steel, Mater. Sci. Eng. A 644 (2015) 171–183.

[10] X. Zhou, K. Li, D. Zhang, X. Liu, J. Ma, W. Liu, Z. Shen, Textures formed in a CoCrMo alloy by selective laser melting, J. Alloys Compd. 631 (2015) 153–164.

[11] Z. Sun, X. Tan, S.B. Tor, W.Y. Yeong, Selective laser melting of stainless steel 316L with low porosity and high build rates, Mater. Des. 104 (2016) 197–204.

[12] X. Zhao, S. Li, M. Zhang, Y. Liu, T.B. Sercombe, S. Wang, Y. Hao, R. Yang, L.E. Murr, Comparison of the microstructures and mechanical properties of Ti–6Al–4V fabricated by selective laser melting and beam melting, Mater. Des. 95 (2016) 21–31.

[13] S. Siegler, J. Toy, D. Seale, D. Pedowitz, The Clinical Biomechanics Award 2013—presented by the International Society of Biomechanics: new observations on the

morphology of the talar dome and its relationship to ankle kinematics, Clin. Biomech. 29 (2014) 1–6.
[14] S. Siegler, J.K. Udupa, S.I. Ringleb, C.W. Imhauser, B.E. Hirsch, D. Odhner, P.K. Saha, E. Okereke, N. Roach, Mechanics of the ankle and subtalar joints revealed through a 3D quasi-static stress MRI technique, J. Biomech. 38 (2005) 567–578.
[15] Y.S. Hedberg, B. Quian, Z. Shen, S. Virtanen, I.O. Wallinder, In vitro biocompatibility of CoCrMo dental alloys fabricated by selective laser melting, Dent. Mater. 30 (2014) 525–534.
[16] E.O. Olakanmi, R.F. Cochrane, K.W. Dalgarno, A review on selective laser sintering/melting (SLS/SLM) of aluminium alloy powders: processing, microstructure, and properties, Prog. Mater. Sci. 74 (2015) 401–477.